Design and synthesis of hierarchical MnO-Fe3O4@C/expanded graphite composite for sensitive electrochemical detection of bisphenol A

Peer-reviewed author version

Zhao, Yao; Zhang, Shu; Yao, Wang; Zhu, Yuxuan; Qian, Jing; Yang , Juan & YANG, Nianjun (2024) Design and synthesis of hierarchical MnO-Fe3O4@C/expanded graphite composite for sensitive electrochemical detection of bisphenol A. In: Talanta, 269 (Art N° 125453).

DOI: 10.1016/j.talanta.2023.125453
Handle: http://hdl.handle.net/1942/42057

Design and synthesis of hierarchical MnO-Fe_3O_4@C/expanded graphite composite for sensitive electrochemical detection of bisphenol A

Yao Zhao[1], Shu Zhang[1], Wang Yao[1], Yuxuan Zhu[1], Jing Qian[1], Juan Yang[1]*, and Nianjun Yang[2, 3]

[1] School of Chemistry and Environmental Engineering, Key Laboratory for Green Chemical Process of Ministry of Education, Hubei Key Lab of Novel Reactor and Green Chemical Technology, Wuhan Institute of Technology, Wuhan 430073, China

[2] Department of Chemistry, Hasselt University, 3590 Diepenbeek, Belgium

[3] IMO-IMOMEC, Hasselt University, 3590 Diepenbeek, Belgium

Abstract

Hierarchically nanostructured binary transition metal oxide-based materials with high conductivity and catalytic activity are quite attractive for the electrochemical quantitative detection of environmental pollutants due to their natural abundance, variable oxidation state, and excellent synergies between metal sites. Herein, a new hierarchical MnO-Fe_3O_4@C/expanded graphite (EG) composite is designed and synthesized through a simple and in situ annealing method with the utilization of bimetallic organic framework (FeMn-MOF)/EG precursor. The synthesized MnO-Fe_3O_4@C/EG composite possesses a unique hierarchical nanoarchitecture that small-sized bimetallic oxide nanoparticles of 10–40 nm completely encapsulated by amorphous carbon layers of 2–4 nm are uniformly distributed on the EG platform. This distinctive structure combines the advantages of high conductivity, excellent catalytic activity, and strong stability. Resultantly, when it is applied to monitor environmental endocrine disruptors, the sensor exhibits a significant catalytic effect on the electrochemical oxidation of bisphenol A (BPA), inducing an amplified response current. In addition, the sensor shows a wide linear range of 1–50 μM and 50–400 μM for the BPA monitor, giving a sensitivity of 5208.8 and 1641.9 μA mM^{-1} cm^{-2}, respectively. This study offers a new approach to design hierarchical binary metal oxide-based sensing materials as well as to explore their electrochemical properties and applications for the determination of emerging contaminants.

Keywords: transition metal oxide; expanded graphite; electrochemical sensor; bisphenol A

*Corresponding author: Juan Yang

E-mail address: jyangchem@wit.edu.cn

1. Introduction

Bisphenol A (BPA) is a kind of endocrine disruptor, which has been identified as an emerging contaminant around the world [1]. It is omnipresent due to its widespread use for commercial product manufacturing, including baby bottles, plastic packaging, food and beverage containers, water pipes, thermal receipts, and so on [2-5]. Resulting from its ubiquitous use, humans may be unintentionally exposed to trace amounts of BPA from drinks, food, or water because of the release and migration from the plastic containers to the food products [6, 7]. The toxic effects of BPA on human′s body have been recognized. In addition to the typical endocrine disrupting effects which interfere with hormonal activities by disrupting growth, development, reproductive, and immune disorders, BPA is suspected to be associated with many diseases such as obesity, diabetes, cardiovascular disease, birth defect, and breast cancer even at a very low concentration [8, 9]. Out of the consideration of human health and ecotoxicology risk, the limitation of BPA in foodstuffs has been regulated by many agencies [7]. Such as that the European Union has already set a dissolution limitation of food exposure to BPA less than 0.05 $mg \cdot kg^{-1}$ in 2016. In Japan, the migration limit of BPA in food containers is established as 2.5 $mg \cdot kg^{-1}$ [2, 6, 10]. Even some countries explicitly forbid the addition of BPA in daily consumption products [11]. Therefore, for the sake of human health and safety, developing a rapid, sensitive, and reliable method for the detection of BPA is a significant task.

The techniques involved ultraviolet, fluorometry, mass spectrometry, and chromatography have been recognized as highly sensitive methods for BPA monitoring [12-14]. However, the expensive instruments and cumbersome sample pretreatment greatly limit their application. In contrast, electrochemical methods are widely used in environmental analysis owing to their characteristics of low cost, instrument simplicity, simple operation, excellent sensitivity, fast response, and real-time in situ analysis [3, 15-20]. Literally, BPA is an electro-active species containing a phenolic structure which is applicable to be monitored using an electrochemical sensor. Nevertheless, the electrochemical oxidation of BPA on a bare electrode is irreversible, resulting in the fouling of the electrode surface. Additionally, the high oxidation potential involved in the detection process will cause unnecessary interference, inducing a low sensing performance. Thus, developing and designing advanced cost-effective catalysts with high catalytic and sensing properties is extremely critical.

Transition metal oxide (TMO)-based sensing materials have played a noteworthy role in fabricating efficient electrochemical sensors due to their natural abundance, high electrochemical activity, variable oxidation state, and unique D-orbital characteristics [21, 22]. Specially, Fe_3O_4 is a widely studied electrode material. Iron is present in the Fe_3O_4 as a bivalent and trivalent oxidation state. The rapid electron transfer between the different valence states makes Fe_3O_4 nanoparticles an excellent electrocatalyst. For instance, Fe_3O_4/poly(amidoamine) nanoparticles, Fe_3O_4/graphene oxide, and Fe_3O_4/carbon nanotubes have been reported as sensing material for the detection of BPA [23, 24]. In recent years, many e orts have been shifted to the development of binary TMO nanostructured materials because they can offer more brilliant electrocatalytic activity in comparison with single-component oxides. The combined binary TMOs are considered as a new class of advanced and promising electrode materials due to their relatively rich redox chemistry and contributions of both metal species in the electrochemical reaction [22, 25]. For instance, He et al. reported a MnO/Fe_3O_4-based electrode material for lithium-ion batteries. The electrochemical performance was greatly enhanced due to the introduction of Mn element [26]. Other similar binary TMOs-based electrocatalysts such as NiO@Fe_3O_4, Mn_3O_4/Fe_3O_4, Co/Fe_3O_4 have also been reported to have superior electrocatalytic properties than that of its single component [27-29]. However, up to present, little information is available about the binary TMO as electroactive materials for the monitoring of BPA contaminant.

Nowadays, many strategies including the solvothermal method, microwave-assisted method, electrodeposition method, and so on have been reported for the preparation of nanostructured binary TMO [30]. Particularly, using metal organic frameworks (MOFs) as sacrificial templates to prepare multitudinous and adjustable binary TMO is accessible due to the diverse composition and tailorable chemical property of MOFs [31]. Through simple calcination in an inert atmosphere, the regularly distributed metal clusters bridged by organic linkers in MOFs can be in situ transformed into small-sized metal oxide. At the same time, the organic ligands can be converted into a stable carbon layer, which is attached to the surface of the metal oxide, thus effectively preventing the migration and dissolution of the active metal species and further improving the stability of the obtained material [26].

Despite a lot of neoteric and advanced binary TMOs have been reported through the MOF-assisted template method, there are still some shortcomings. On the one hand, the single MOF precursor generally suffer from the issue of agglomerate growth, resulting in the agglomerated binary TMOs [31]. The aggregated TMOs often display humble electrochemical activity due to the low specific surface area and limited exposed active sites. On the other hand, despite MOF-derived products possessing a carbon layer, the obtained carbon generally has inferior electrocatalytic activity. Meanwhile, the inherent low electrical conductivity of TMO cannot be effectively improved through the slight MOF-derived carbon. In this regard, an effective strategy to remedy these deficiencies is to introduce a good conductivity matrix platform to anchor and disperse active species. Expanded graphite (EG) is a promising choice as the carbon supporter as it possesses high conductivity, large surface area, high stability, facile and cut-price production, and special catalytic activity [32]. Once the EG is used as a growth platform for MOF precursor tailoring its structure, the aggregation growth of MOF will be refined, gaining effective TMO/EG sensing material.

Thus, in this work, MnO-Fe_3O_4@C/EG composite was designed and prepared through a simple one-step annealing of the FeMn-MOF/EG precursor in the N_2 atmosphere. The morphology, chemical structure, and electrochemical activity of the hierarchical MnO-Fe_3O_4@C/EG composite were explored. The coupling ratio of Fe/Mn in the hierarchical structure was reasonably optimized. Moreover, the developed MnO-Fe_3O_4@C/EG composite was constructed as a novel electrochemical sensor for the sensitive and selective detection of BPA. Eventually, the sensor was applied to monitor BPA in a commercially available plastic water bottle.

2. Experimental

2.1. Reagents and materials

$FeCl_3$, $Mn(CH_3COO)_2 \cdot 4H_2O$, HNO_3, $Na_2HPO_4 \cdot 12H_2O$, $NaH_2PO_4 \cdot 2H_2O$, acetic anhydride, and N, N-dimethylformamide (DMF) were bought from Sinopharm Chemical Reagent Co. Ltd. (Beijing, China). Urea, bisphenol S, catechol, hydroquinone, 2-nitrophenol, 4-nitrophenol, resorcinol, bisphenol A (BPA), 1,4-benzenedicarboxylic acid (H_2BDC) and bisphenol A (BPA) were purchased from Aladdin Chemistry Co. Ltd. (Shanghai, China). All chemicals and agents with analytical grade were directly used without any treatment.

Phosphate buffer solutions (PBS) with different pH values were prepared by appropriately mixing 0.10 M Na_2HPO_4 solution and 0.10 M NaH_2PO_4 solution. Ultrapure water came from a Milli-Q water purification system (Millipore, USA) and was used thoroughly in the whole experiment process.

2.2. Instruments

Field-emission scanning electron microscopy (FESEM, JEOL-JSM-7100F, Japan) and transmission electron microscopy (TEM, Tecnai G2 20 S-TWIN, USA) were adopted to characterize the morphologies and microstructures of as-prepared samples. Powder X-ray diffraction (XRD) patterns were provided by a Bruke D8 diffractometer operated at 300 mA and 40 kV with Cu Kα radiation (Germany). X-ray photoelectron spectroscopy (XPS) measurements were carried out on an AXIS-UL TRA DLD-600W spectrometer (SHIMADZU-Kratos Company, Japan). Electrochemical measurements including cyclic voltammetry (CV), Differential pulse voltammetry (DPV), and electrochemical impedance spectroscopy (EIS) were investigated through a CHI760E electrochemical analyzer (Chenhua Inc., Shanghai, China).

2.3. Preparation of FeMn-MOF/EG

Firstly, EG was prepared via the microwave oxidation of natural graphite flake [32]. To obtain EG, concentrated HNO_3 and acetic anhydride were operated as oxidizing agents while chlorate acted as an intercalation agent. The mixed reagent was placed in a microwave reactor and executed at 700 W for 30 s. After repeated centrifugation and cleaning, EG was obtained.

The FeMn-MOF/EG composite was prepared according to the reported literature with minor modifications [26]. Briefly, 90 mg EG was dispersed in a 75 mL mixture solution which consisted of 60 mL DMF and 15 mL water with the aid of ultrasonic agitation. Subsequently, $FeCl_3$ (2.25 mM), $Mn(CH_3COO)_2{\cdot}4H_2O$ (2.25 mM), H_2BDC (4.5 mM), and urea (0.45 g) were added in the EG suspension and stirred for 0.5 h to form a homogenous solution. The resultant solution was then transferred into a Teflon-lined stainless steel autoclave and heated at 180°C for 3 h. The product was centrifuged and washed several times with water and ethanol, and finally dried at 80°C overnight. The obtained powder was labeled as FeMn-MOF/EG, referred to the stoichiometric addition of Fe/Mn with a ratio of 1:1. For comparison, pure FeMn-MOF was prepared via the same procedure without EG. To investigate the influence of different metal ratios, other control samples with

the stoichiometric addition of Fe/Mn to 2:1, 1:2, 3:0, and 0:3 were also synthesized through a similar procedure. The corresponding products were labeled as FeMn-MOF/EG (2:1), FeMn-MOF/EG (1:2), Fe-MOF/EG (3:0), and Mn-MOF/EG (0:3), respectively.

2.4. Preparation of MnO-Fe_3O_4@C/EG

The as-synthetized samples were transferred into an alumina boat and subsequently calcined at 700°C for 2 h at a heating rate of 5°C min^{-1} [26]. The pyrolysis was performed in a tube furnace with N_2 atmosphere. Finally, the FeMn-MOF/EG, FeMn-MOF/EG (2:1), FeMn-MOF/EG (1:2), FeMn-MOF, Fe-MOF/EG (3:0), and Mn-MOF/EG (0:3) were converted to MnO-Fe_3O_4@C/EG, MnO-Fe_3O_4@C/EG (2:1), MnO-Fe_3O_4@C/EG (1:2), MnO-Fe_3O_4@C, Fe_3O_4@C/EG (3:0), and MnO@C/EG (0:3), respectively.

2.5. Electrochemical measurements

To prepare the modified electrode, a glassy carbon electrode (GCE, 3.0 mm in diameter) was prior to polished and cleaned. Subsequently, 5.0 μL of the 2 mg mL^{-1} sample suspension was dropped onto the pretreated GCE and dried in an air atmosphere under an infrared lamp.

All electrochemical experiments were carried out using a conventional three-electrode system in which a bare GCE or modified GCE was used as the working electrode, a platinum wire was applied for the counter electrode, and a saturated calomel electrode (SCE) was regarded as the reference electrode. The supporting electrolyte was supplied by 0.10 M PBS.

CVs of the modified GCEs in 10.00 mL PBS with definite concentration of BPA were recorded in the potential range of 0.2 — 0.7 V (*vs*. SCE). Electrochemical linear detection of BPA was investigated on a MnO-Fe_3O_4@C/EG/GCE modified electrode via DPV technique. Unless otherwise specified, all electrochemical measurements were conducted in a pH 8.0 PBS. EIS of the sensor was carried out in 0.10 M KCl containing 5 mM $[Fe(CN)_6]^{3-/4-}$ redox probe. All experiments were tested at room temperature.

2.6. Sample preparation

The plastic water bottle was bought from the local supermarket (Wuhan, China). The plastic sample was cut into small pieces and then cleaned with water. After drying at room temperature, 2 g chopped samples were

placed in 50 mL ethanol and heated at 50°C for 4 h. Afterward, the pieces were separated, and the filtrate was collected and stored in the refrigerator for further experiment.

3. Result and discussion

3.1. Morphological and structural characterization

The strategy for preparing the hierarchical MnO-Fe_3O_4@C/EG composite is depicted in **Scheme 1**. EG was initially synthesized by microwave oxidation. Through the oxidation — intercalation process, the stacking of graphite flakes is greatly reduced and the spacing between adjacent layers of graphite is enlarged, inducing the increased specific surface area and catalytic ability of EG. Subsequently, EG was used as a platform to provide anchoring sites for bimetallic MOF growth, which was prepared via solvothermal reaction using $FeCl_3$, $Mn(CH_3COO)_2$ $4H_2O$, H_2BDC, and urea as raw reagents. The introduction of urea can accelerate the solubility of H_2BDC and promote the formation of FeMn-MOF [26]. During the annealing treatment of FeMn-MOF/EG in an inert atmosphere, the Fe^{3+} and Mn^{2+} ions were transformed into Fe_3O_4 and MnO, and the organic ligand H_2BDC was carbonized to C to encapsulate the metal oxides, leading to the formation of the hierarchical MnO-Fe_3O_4@C/EG composite.

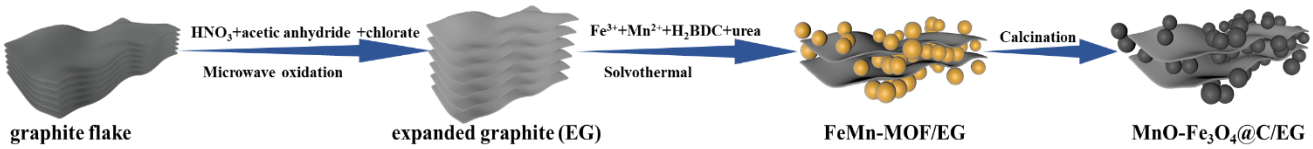

Scheme 1 Schematic illustration for the fabrication of hierarchical MnO-Fe_3O_4@C/EG.

The structural morphologies of FeMn-MOF/EG precursor and the resulting MnO-Fe_3O_4@C/EG composite were characterized by SEM and TEM, as illustrated in **Fig.1** and **Fig. S1** (the Supporting Information). In the SEM image of FeMn-MOF/EG precursor, EG is composed of large sheets featuring a typical wrinkled structure with smooth surface. Some aggregated FeMn-MOF nanoparticles are attached to the surface of EG (**Fig. S1**). After the high-temperature calcination, the morphology of the precursor was well-maintained, and the metal oxide nanoparticles are uniformly distributed on the surface of EG (**Fig. 1a-b**). From the enlarged vision, it can be seen that the black nanoparticles with a diameter of 10—40 nm have a heterogeneous structure

and all the nanoparticles are completely encapsulated by a layer of amorphous carbon with a thickness of 2—4 nm (**Fig. 1c**). This heterogeneous structure can provide high conductivity and effectively prevent the agglomeration of nanoparticles, resulting in a stable and efficient catalytic interface for the electrochemical sensing application. Moreover, the representative high-magnification TEM image confirms the presence of Fe_3O_4 and MnO in the resulting MnO-Fe_3O_4@C/EG composite (**Fig. 1d**). The black nanoparticles demonstrate clear lattice fringes with distances of 2.21 and 2.53 Å, which agree well with the lattice spacing of the (200) plane of MnO and the (311) crystal plane of Fe_3O_4, respectively [26, 33, 34]. From the EDS results, it can be demonstrated that the MnO-Fe_3O_4@C/EG composite is composed of Fe, Mn, C, and O elements, and all elements are uniformly distributed (**Fig. 1e**).

The phase structure of the MnO-Fe_3O_4@C/EG and MnO-Fe_3O_4@C was characterized by XRD characterization. As displayed in **Fig.2**, the XRD spectrum of MnO-Fe_3O_4@C/EG exhibits strong characteristic peaks at 2θ = 26.46° and 44.74°, corresponding to the (002) and (101) of EG, respectively. Other diffraction peaks can be well assigned to MnO (JCPDS No. 3-1145) and cubic spinel Fe_3O_4 (JCPDS No. 65-3107) [26, 35]. These results confirm the presence of heterogeneous EG, MnO, and Fe_3O_4 in the annealed product. As for the MnO-Fe_3O_4@C, all the peaks can be credited to MnO and Fe_3O_4 and no distinct peaks corresponding to carbon is observed, probably due to the low content of amorphous carbon layer. In addition, the intensity corresponding to the diffraction peak of MnO in MnO-Fe_3O_4@C/EG is relatively more intuitive than that of MnO-Fe_3O_4@C, which implies that the introduction of EG may be conducive to improving the crystallinity of MnO in the composite.

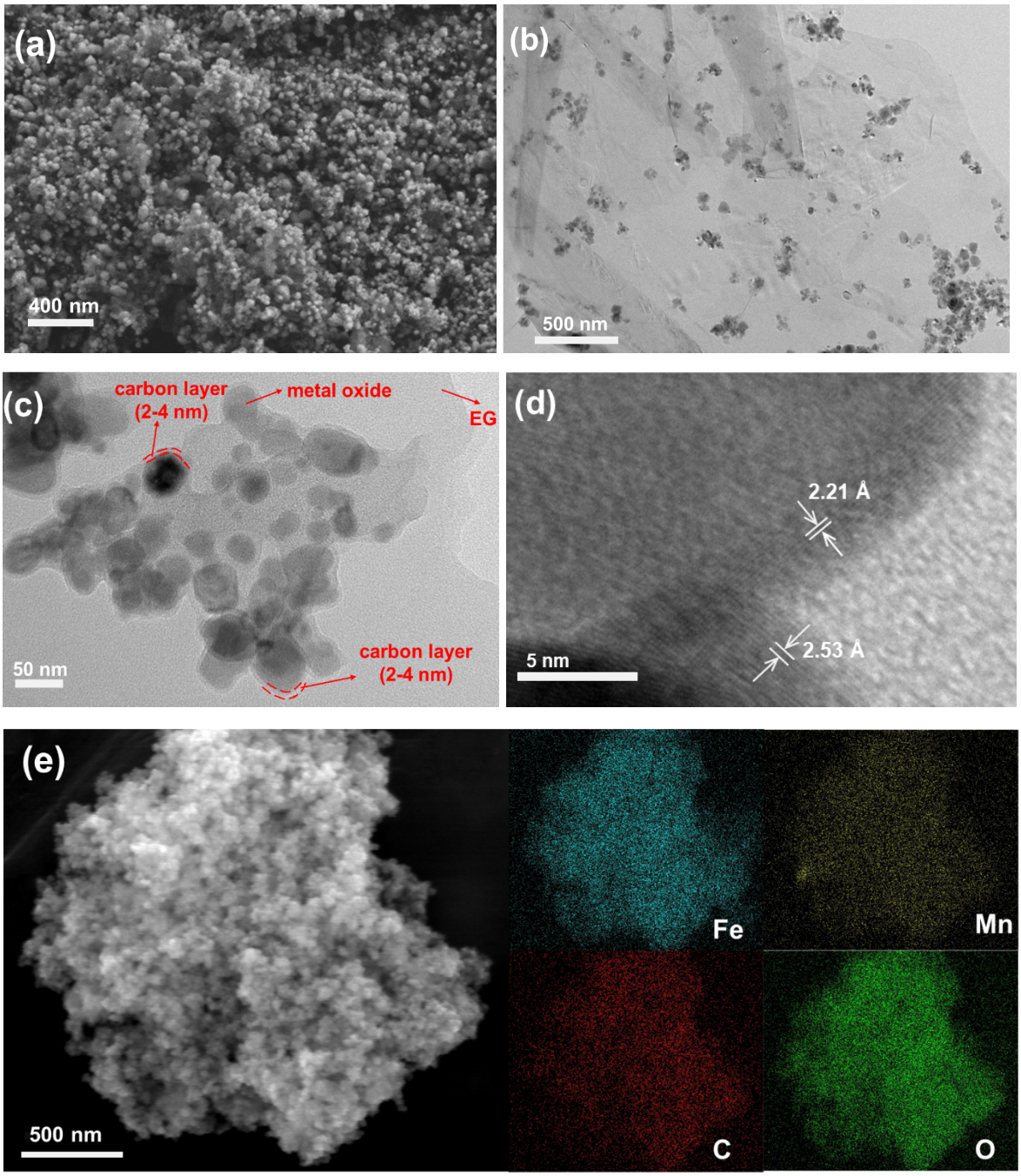

Fig.1 SEM image (a), TEM images at different magnifications (b-c), and high-magnification TEM image (d) of MnO-Fe_3O_4@C/EG; EDS elemental mapping of Fe, Mn, C, and O for the MnO-Fe_3O_4@C/EG composite (e).

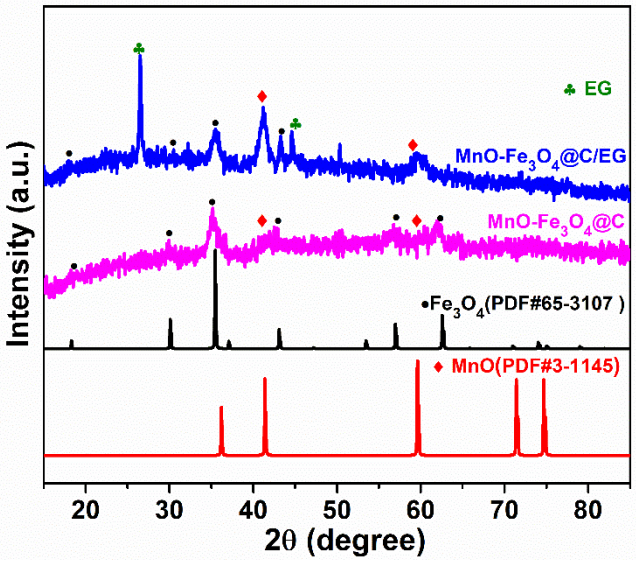

Fig.2 XRD patterns of MnO-Fe_3O_4@C/EG, MnO-Fe_3O_4@C, simulated Fe_3O_4, and simulated MnO.

Moreover, XPS analysis was conducted to analyze the chemical composition and valence states of MnO-Fe_3O_4@C/EG and MnO-Fe_3O_4@C. In the wide-scan XPS survey spectra, the presence of C, O, Mn, and Fe elements is confirmed in both samples (**Fig.3a**). The Fe/Mn atomic ratio index is calculated as 1.33 for MnO-Fe_3O_4@C/EG and 1.92 for MnO-Fe_3O_4@C. The slightly lower value for MnO-Fe_3O_4@C/EG indicates a certain advantage of EG in fixing MnO. The high-resolution C 1s XPS spectra for both MnO-Fe_3O_4@C/EG and MnO-Fe_3O_4@C can be fitted into three peaks, which are located at about 284.6, 286.1, and 288.7 eV, assigned to C-C, C-O, and C=O species, respectively (**Fig.3b**) [36]. In the high-resolution Mn 2p XPS spectrum of MnO-Fe_3O_4@C, two characteristic peaks at 641.9 and 653.2 eV can be ascribed to Mn $2p_{3/2}$ and Mn $2p_{1/2}$ of MnO, respectively [37]. For the MnO-Fe_3O_4@C/EG, both the Mn $2p_{3/2}$ and Mn $2p_{1/2}$ peaks lying at 641.4 and 652.8 eV shift to lower binding energies (BEs), giving the gaps of 0.4—0.5 eV (**Fig.3c**). The Fe 2p XPS spectrum of MnO-Fe_3O_4@C includes two shakeup satellite peaks (718.7 and 732.6 eV) and a double peak credited to Fe $2p_{3/2}$ and Fe $2p_{1/2}$. Both Fe $2p_{3/2}$ and Fe $2p_{1/2}$ are curve-fitted. Two characteristic peaks with the BEs of 710.8 and 724.1 eV are assigned to Fe^{2+}, and the other two specific peaks with the BEs of 713.1 and 726.7 eV belong to Fe^{3+} (**Fig.3d**) [38, 39]. The MnO-Fe_3O_4@C/EG exhibits a similar Fe 2p XPS spectrum with a decreased Fe^{3+} spectrum area reducing from 53.3% to 52.3% and a negative shift in the BEs of both Fe^{2+} (710.5 and 723.8 eV) and Fe^{3+} (712.9 and 726.3 eV). Generally, the BEs shift of metallic species and the decreased Fe^{3+} proportion

may be attributed to the strong electronic interaction between MnO and Fe_3O_4. On the other hand, charge transfer could occur between the metal oxide and EG. This will enhance the electronic conductivity of the catalyst and facilitate the reaction kinetics of the sensing interface [26].

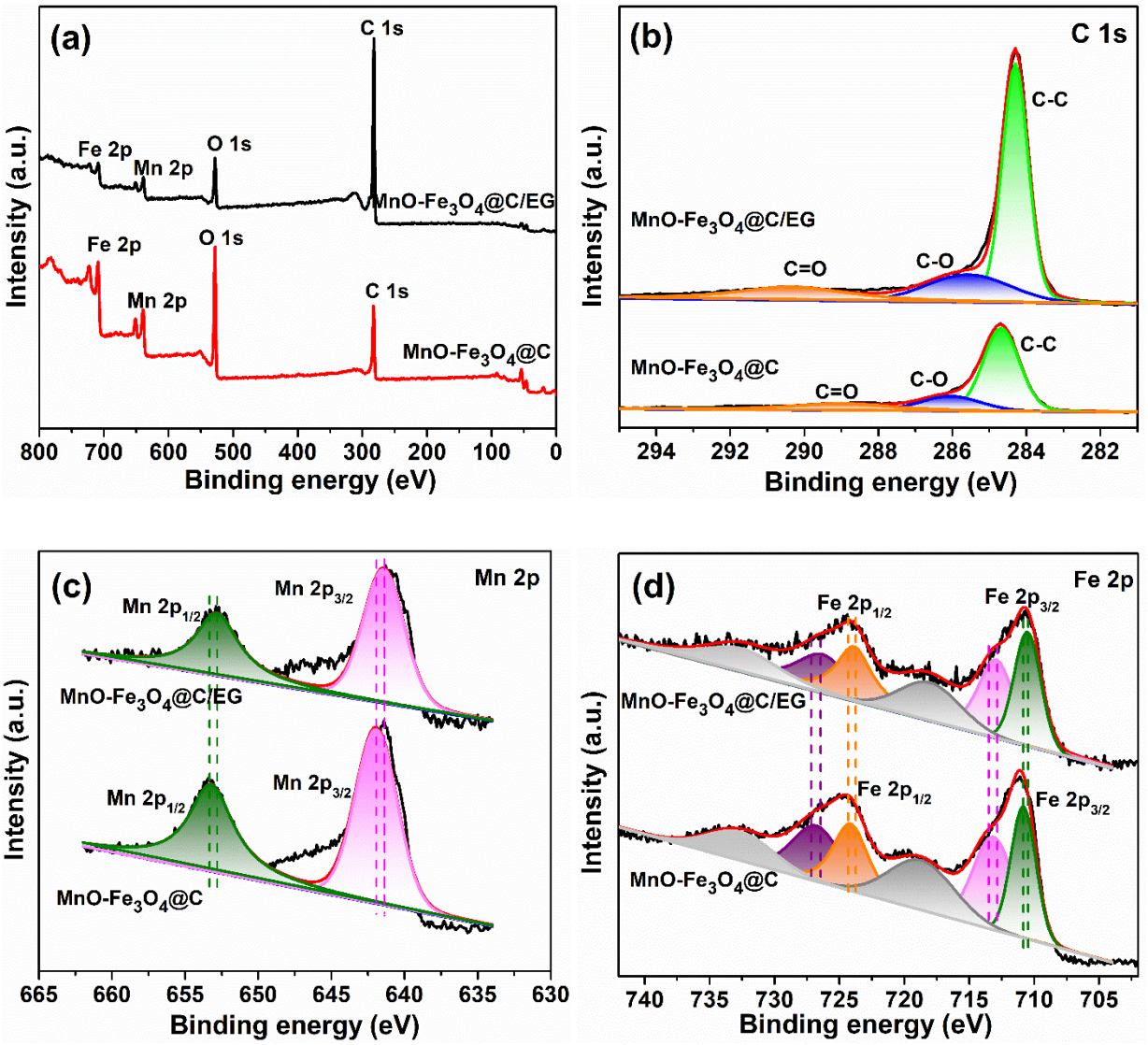

Fig.3 Survey XPS spectrum (a) and high resolution XPS spectra of C 1s (b), Mn 2p (c), and Fe 2p (d) of MnO-Fe_3O_4@C and MnO-Fe_3O_4@C/EG.

3.2. Electrochemical assessments

The electrochemical property of bare GCE, EG/GCE, MnO-Fe_3O_4@C/GCE, and MnO-Fe_3O_4@C/EG/GCE modified electrodes was recorded in 5 mM $[Fe(CN)_6]^{3-/4-}$ redox probe by means of CV and EIS. As shown in

Fig.4a, a pair of well-defined CV redox peaks assigned to the conversion of Fe (III)/Fe (IV) species are observed on all modified electrodes [40]. Under the same conditions, the anodic peak currents (I_{pa}) follow a sequence of MnO-Fe_3O_4@C/EG/GCE (163.7 μA) > EG/GCE (123.4 μA) > MnO-Fe_3O_4@C/GCE (114.3 μA) > GCE (86.7 μA). Compared with that of bare GCE, both EG/GCE and MnO-Fe_3O_4@C/GCE exhibit a higher peak current due to their higher electrochemical activity. In addition, MnO-Fe_3O_4@C/EG/GCE possesses the best electrochemical response and reversibility corresponded to the peak-to-peak separation (ΔE_p) of 101 mV probably due to the synergistic effects of EG and MnO-Fe_3O_4@C. Meanwhile, the electrochemically active surface area (ECSA) of these electrodes was also explored by recording CV curves in the $[Fe(CN)_6]^{3-/4-}$ probe ranging from 30 to 180 mV s^{-1} (**Fig.S2**). According to the Randles–Sevcik equation [41, 42], the ECSAs of bare GCE, EG/GCE, MnO-Fe_3O_4@C/GCE, and MnO-Fe_3O_4@C/EG/GCE are calculated as 0.126, 0.133, 0.143, and 0.175 cm^2, respectively.

The Nyquist plots of modified electrodes fitted with the Randles equivalent circuit are presented in **Fig.4b**. Usually, the semicircular part at higher frequency region is allocated to the electron transfer process while the linear portion at lower frequency region can be credited to the diffusion process [43]. According to the diameter of the semicircle, the electron-transfer resistance (R_{ct}), which is indicative of conductivity, can be evaluated. Compared with bare GCE of 238.5 Ω, EG, MnO-Fe_3O_4@C, and MnO-Fe_3O_4@C/EG composite achieve lower R_{ct} of 115.8 Ω, 133 Ω, and 81.91 Ω, respectively, indicating their high conductivity. Since the R_{ct} of MnO-Fe_3O_4@C/EG composite is the lowest, it features the fastest electron-transfer rate between the electrode interface and the analyte, which is favorable to the improvement of selectivity.

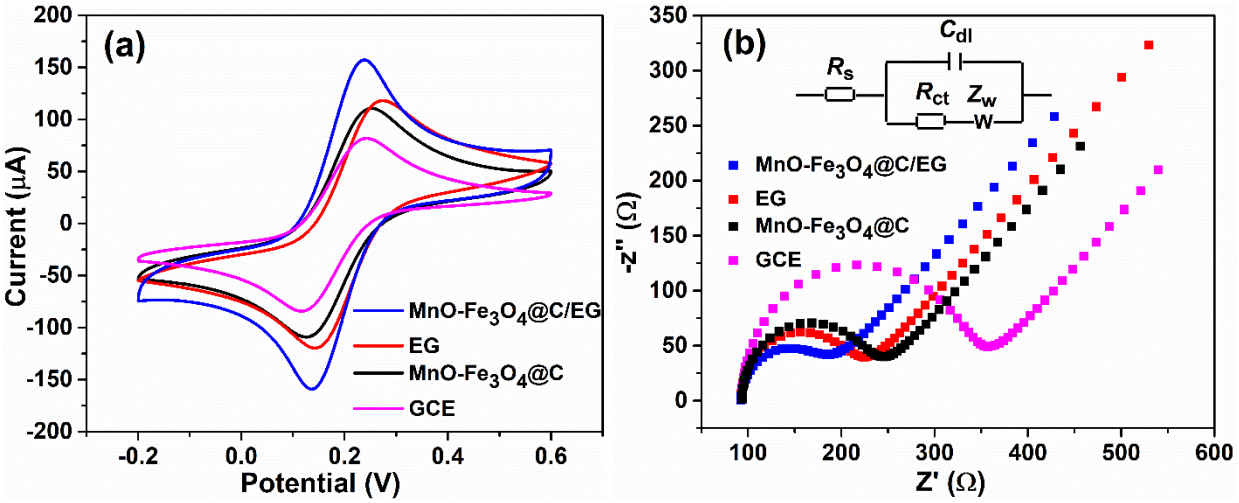

Fig.4 CVs (a) and Nyquist plots (b) of the various electrodes in 0.1 M KCl containing 5 mM $[Fe(CN)_6]^{3-/4-}$. The inset in (b) is Randles equivalent circuit, where Rs, Zw, and Cdl represent the electrolyte solution resistance, Warburg component, and double layer capacitance, respectively [40].

3.3. Electrocatalytic detection of BPA

The electrochemical responses of BPA on various modified electrodes were investigated by CV at 50 mV s^{-1}. As shown in **Fig. 5a**, no obvious redox peak is found at all electrodes in 0.1 M pH 8.0 PBS. Upon the addition of 50 μM BPA in PBS, bare GCE exhibits a poor sensitivity toward BPA accompanying a wide and small oxidation peak of 2.537 μA at 0.499 V. Obviously, both EG/GCE and MnO-Fe_3O_4@C/GCE show a superior catalytic activity to BPA, reflecting in the negative shift of oxidation peak potential (0.457 and 0.467 V) and comparatively large peak current (8.087 and 6.867 μA). It is noteworthy that MnO-Fe_3O_4@C/EG/GCE yields the largest oxidation peak current and the smallest anodic peak potential (E_{pa}) of 16.14 μA at 0.420 V, which may be attributed to the excellent electron transfer ability of the MnO-Fe_3O_4@C/EG composite and the synergetic catalytic effect between MnO-Fe_3O_4@C and EG.

For comparison, the oxidation signals of MnO-Fe_3O_4@C/EG composites with different Fe/Mn ratios to BPA were also explored. In this regard, five different composites with the Fe/Mn ratios of 3:0, 2:1, 1:1, 1:2, and 0:3 were synthesized. As illustrated in **Fig. 5b**, the anodic peak current of 50 μM BPA on Fe_3O_4@C/EG (3:0), MnO-Fe_3O_4@C/EG (2:1), MnO-Fe_3O_4@C/EG (1:1), MnO-Fe_3O_4@C/EG (1:2), and MnO@C/EG (0:3) is 9.947, 13.58, 16.14, 3.339, and 5.036 μA, respectively. Apparently, the MnO-Fe_3O_4@C/EG referred to 1:1 possesses

the largest current, suggesting that MnO-Fe_3O_4@C/EG is more sensitive than that of the composites composed of only a single metal. In addition, the peak potential is slightly negative -shifted with the increase of iron content in the composite. These results suggest an indication of the excellent electrocatalytic performance of iron species to BPA and the synergistic effect between different metal oxides. Therefore, MnO-Fe_3O_4@C/EG is considered to be the most promising sensing material for the monitoring of BPA.

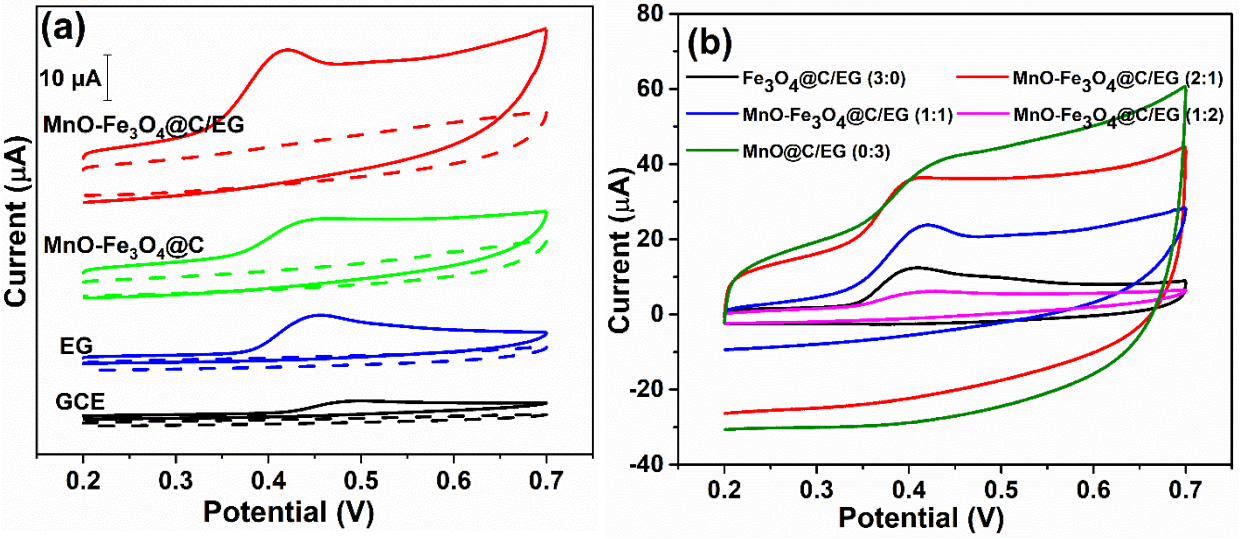

Fig.5 (a) CVs of different modified electrodes in absence (dotted line) and presence (solid line) of 50 μM BPA in 0.1 M pH 8.0 PBS; (b) CVs of 0.1 M pH 8.0 PBS with 50 μM BPA on MnO-Fe_3O_4@C/EG composites with different Fe/Mn ratios.

To further analyze the electrode kinetic of BPA on MnO-Fe_3O_4@C/EG/GCE, different scan rates (50 — 300 mV s^{-1}) were applied to explore the electrochemical behavior of BPA. The superimposed CVs are presented in **Fig.6a**. It can be seen that the peak currents appear to gradually increase with the growing scan rate. After linear fitted, a good linear relationship between peak current and scan rate (v) is noticed, following a linear equation of $I_{pa} = 0.026v + 0.811$ ($R^2 = 0.9910$) (Fig.6b). This result confirms that the electrochemical oxidation of BPA on MnO-Fe_3O_4@C/GCE is an adsorption-controlled process [44]. Meanwhile, the peak potentials tend to positive shift with the increase of scan rate, conforming to a regression equation of $E_{pa} = 0.023\ln v + 0.333$ ($R^2 = 0.9915$) (**Fig.6b**). According to the Laviron's theory, the electron-transfer number (n) is calculated to be

2 while the electron-transfer coefficient (α_s) is usually assumed to be 0.5 for an irreversible electrode process [45].

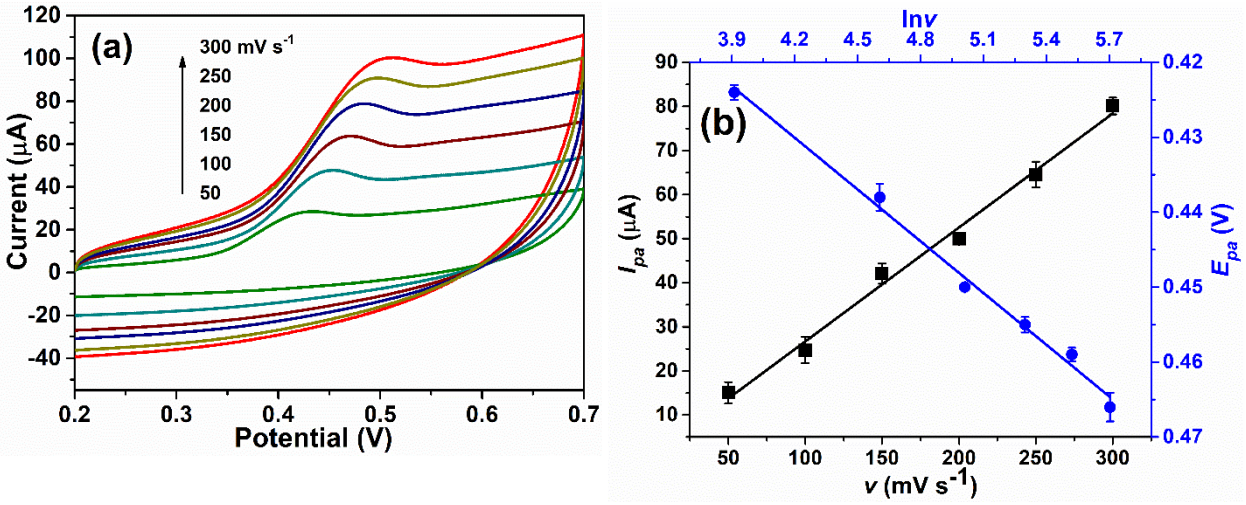

Fig.6 (a) CVs of 50 μM BPA on MnO-Fe_3O_4@C/EG/GCE at different scan rates in 0.10 M pH 8.0 PBS; the plots of I_{pa} versus v and E_{pa} versus ln$v$ (b).

The pH of PBS is an important factor that affects the acid-base dissociation of BPA, which will cause a change in its oxidation current and potential. The CVs of 50 μM BPA on MnO-Fe_3O_4@C/EG/GCE in 0.1 M PBS with pH ranged from 7.0 — 9.0 at 100 mV s^{-1} were recorded in **Fig.7a**. The response current increases with the pH changing from 7.0 to 8.0, but further increase will bring a decreased current (**Fig.7b**). In this case, pH of 8.0 is chosen as the best medium environment. Moreover, the E_{pa} value linearly shifts towards the negative potential with an increase of pH value obeying the linear regression equation of E_{pa} = -0.0522 pH +0.834 (R^2 = 0.9912). The absolute slope value is 52.2 mV pH^{-1}, which is close to the theoretical Nernst value of 59 mV pH^{-1}. Since the electron-transfer number obtained from the above study on scan rate effect is 2, it is therefore concluded that the electrochemical oxidation reaction of BPA on MnO-Fe_3O_4@C/EG/GCE involves the transfer of two electrons and protons, which is consistent with previously reported results [45]. The possible electrochemical oxidation mechanism of BPA is offered in Eq.1.

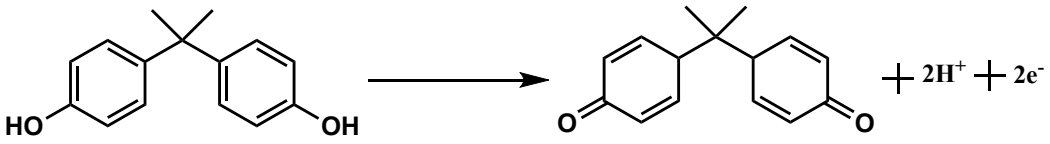

(Eq.1)

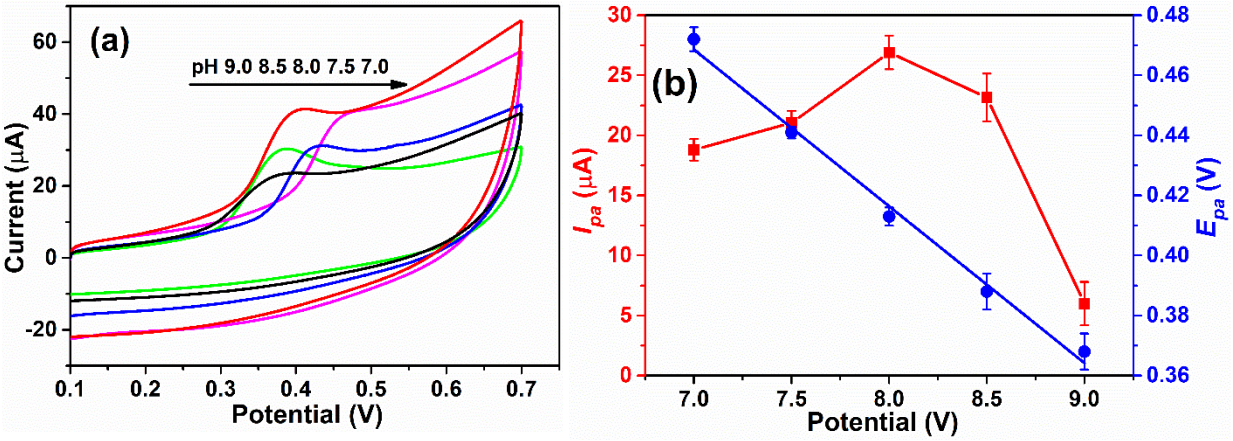

Fig.7 (a) CVs of 50 μM BPA on MnO-Fe_3O_4@C/EG/GCE in 0.1 M PBS with different pH values; (b) Relationship between I_{pa}/E_{pa} and pH value.

In order to achieve the best sensitivity, relevant parameters including accumulation time, accumulation potential, and the amount of MnO-Fe_3O_4@C/EG were optimized. When the accumulation time varies in the range of 1— 6 min, the I_{pa} enhances first and then decreases. A maximum value is reached at 4 min (**Fig.S3a**). The same trend occurs when the accumulation potential changes from 0.0 to 0.4 V, and the top I_{pa} value is obtained at 0.2 V (**Fig.S3b**). The amount of MnO-Fe_3O_4@C/EG catalyst was adjusted by changing the volume of MnO-Fe_3O_4@C/EG dispersion. When the volume increases from 2.0 to 6.0 μL, the I_{pa} of BPA enhances gradually up to 5.0 μL, then it decreases (**Fig.S3c**). This is associated with the effective electrode active area and electron transfer resistance. Therefore, an accumulation time of 4 min, an accumulation potential of 0.2 V, and 5.0 μL MnO-Fe_3O_4@C/EG dispersion were applied as the optimal experimental conditions.

Under these optimal conditions, the DPV curves of different BPA at MnO-Fe_3O_4@C/EG/GCE were recorded (**Fig.8a**). The I_{pa} increases upon the increase of BPA concentration and possesses a two linear relationship with the BPA concentrations (**Fig.8b**). The linear equations are I_{pa} = 0.368 C + 0.305 (R^2 = 0.9936) and I_{pa} = 0.116 C + 13.089 (R^2 = 0.9952) corresponding to the concentration range of 1—50 and 50—400 μM, respectively. The sensitivity is calculated as 5208.8 and 1641.9 μA mM^{-1} cm^{-2} assigned to the low and high concentration range, respectively. The limit of detection (LOD) is 0.7 μM based on the threefold signal-to-noise ratio (S/N = 3). Compared with the sensing performance of previously reported electrochemical sensors

for BPA monitoring, the proposed MnO-Fe_3O_4@C/EG/GCE displays a comparable sensitivity and wide linear range (**Table 1**).

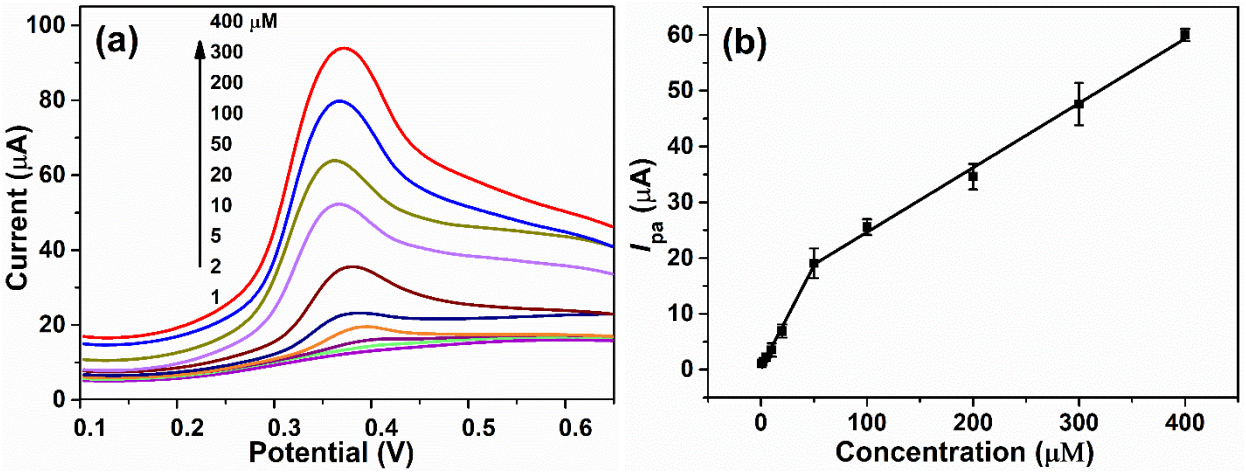

Fig.8 (a) DPVs of BPA in 0.1 M pH 8.0 PBS on MnO-Fe_3O_4@C/EG/GCE with different concentrations; (b) calibration plot of peak current versus BPA concentrations.

The selectivity ability of MnO-Fe_3O_4@C/EG/GCE for the detection of BPA was evaluated in the presence of some interfering substances. The equivalent organic compounds such as bisphenol S, catechol, hydroquinone, 2-nitrophenol, 4-nitrophenol, and resorcinol possess negligible interference with the relative standard deviations (RSDs) of the current response below 5.0%. Apart from the selectivity, the reproducibility and repeatability were also investigated. Six MnO-Fe_3O_4@C/EG/GCE modified electrodes were prepared independently and used to monitor BPA. The RSD was calculated to be 4.8% (n=7). Moreover, six successive measurements using a MnO-Fe_3O_4@C/EG/GCE electrode gave RSDs of 2.8% (n=7). These results demonstrate that the sensor has good selectivity, reproducibility, and repeatability and is suitable for the determination of BPA in real samples.

The application feasibility of MnO-Fe_3O_4@C/EG was validated by quantitatively monitoring the concentration of BPA in a real sample of a plastic water bottle (**Table 2**). The results show that no BPA is found, implying the safety of the plastic water bottle. Moreover, the accuracy of the developed method was assessed by recovery test through the standard addition method. As a result, the spiking recovery for various concentrations of BPA standards added is 98.90%–103.0% (n=3), indicating that this method is reliable.

Table 1 Comparison of the developed sensor with other reported electrochemical sensors for the determination of BPA

Sensor	Sensitivity (μA $μM^{-1}$)	Linear range (μM)	LOD (μM)	Ref.
Cu_2O-rGO/GCE	3.504	0.1—80	0.053	[4]
MWCNTs-βCD/SPCE	2.159	0.125—2	0.0137	[46]
	7.194	2—30		
$NiFe_2O_4$-rGO/SPCE	0.6132	0.05—25	0.01	[47]
Ce-Zn-MOF/MWCNT/GCE	0.5422	0.1—100	0.0072	[48]
COF (CTpPa-2)/GCE	0.1263	0.1—2.5	0.02	[49]
	0.0501	2.5—50		
Au/COF/GCE	0.5831	5—1000	1	[15]
MnO-Fe_3O_4@C/EG/GCE	0.116	1—50	0.7	This work
	0.368	50—400		

rGO: reduced graphene oxide; βCD/SPCE:β-cyclodextrin/screen-printed carbon electrode; COF (CTpPa-2): covalent organic framework synthesized with functionalized 1,3,5-triformylphloroglucinol and 2,5-dimethyl-p-phenylenediamine

Table 2 Determination of BPA in a real sample with a MnO-Fe_3O_4@C/EG/GCE

Sample	Added (μM)	Found (μM)	Recovery (%)	RSD (%)
plastic water bottle	0	Not Found	-	1.7
	50.00	49.45	98.90	3.1
	80.00	80.84	101.0	2.5
	100.0	102.98	103.0	3.4

4. Conclusion

In summary, a unique and hierarchical MnO-Fe_3O_4@C/EG composite was successfully synthesized through a simple in situ annealing of FeMn-MOF/EG precursor. The introduction of EG significantly enhances the conductivity of the hierarchical composite. Moreover, the distinct architecture of the binary TMO encapsulated within an in situ generated carbon layer network contributes to the heightened catalytic activity and stability. This can be attributed to the synergistic effect between the components and the protective nature of the carbon layer. As the coupling ratio of Fe/Mn was optimized as 1:1, the electronic structure of the MnO-Fe_3O_4@C/EG composite is modulated. Consequently, the resulting sensor shows improved electrochemical performance for the determination of BPA with a high sensitivity, wide linear response, low detection limit, and good repeatability. The sensor also displays the feasibility of practical application in plastic products with satisfactory recovery. This work enriches the variety of hierarchical electrocatalysts and provides a reliable new approach for the sensitive detection of environmental contaminants. However, the MOF precursor with different constructs inevitably leads to diverse TMO-based catalytic material, and their relationship may be worth further exploring.

Declaration of competing interest

The authors declare that they have no known competing financial interests or personal relationships that could have appeared to influence the work reported in this paper.

Acknowledgments

This work was supported by the Innovation and Entrepreneurship Training Program for College Students of Hubei Province (No.S202110490008), Student President Fund of Wuhan Institute of Technology (No. xzJJ2021061), Youths Science Foundation of Wuhan Institute of Technology (No. K2021069), and Hubei Key Laboratory of Pollutant Analysis and Reuse Technology (Hubei Normal University) (No.PA220201).

Appendix A. Supplementary data

Supplementary data to this article can be found online at

References

[1] S. Tajik, H. Beitollahi, F.G. Nejad, K. Zhang, Q.V. Le, H.W. Jang, S.Y. Kim, M. Shokouhimehr, Recent advances in electrochemical sensors and biosensors for detecting bisphenol A, Sensors, 20 (2020) 3364.

[2] Y. Zhang, Y. Lei, H. Lu, L. Shi, P. Wang, Z. Ali, J. Li, Electrochemical detection of bisphenols in food: A review, Food Chem., 346 (2021) 128895.

[3] C. Cheng, S. Wang, J. Wu, Y. Yu, R. Li, S. Eda, J. Chen, G. Feng, B. Lawrie, A. Hu, Bisphenol A sensors on polyimide fabricated by laser direct writing for onsite river water monitoring at attomolar concentration, ACS Appl. Mater. Inter., 8 (2016) 17784-17792.

[4] R. Shi, J. Liang, Z. Zhao, A. Liu, Y. Tian, An electrochemical bisphenol A sensor based on one step electrochemical reduction of cuprous oxide wrapped graphene oxide nanoparticles modified electrode, Talanta, 169 (2017) 37-43.

[5] J. Rajendran, T.S. Kannan, L.S. Dhanasekaran, P. Murugan, R. Atchudan, Z.A. Alothman, M. Ouladsmane, A.K. Sundramoorthy, Preparation of 2D graphene/MXene nanocomposite for the electrochemical determination of hazardous bisphenol A in plastic products, Chemosphere, 287 (2022) 132106.

[6] M.K. Alam, M.M. Rahman, A. Elzwawy, S.R. Torati, M.S. Islam, M. Todo, A.M. Asiri, D. Kim, C. Kim, Highly sensitive and selective detection of Bis-phenol A based on hydroxyapatite decorated reduced graphene oxide nanocomposites, Electrochimi. Acta, 241 (2017) 353-361.

[7] A.U. Alam, M.J. Deen, Bisphenol A electrochemical sensor using graphene oxide and β-cyclodextrin-functionalized multi-walled carbon nanotubes, Anal. Chem., 92 (2020) 5532-5539.

[8] Z. Ye, Q. Wang, J. Qiao, B. Ye, G. Li, Simultaneous detection of bisphenol A and bisphenol S with high sensitivity based on a new electrochemical sensor, J Electroanal. Chem., 854 (2019) 113541.

[9] Q. Yang, X. Wu, H. Peng, L. Fu, X. Song, J. Li, H. Xiong, L. Chen, Simultaneous phase-inversion and imprinting based sensor for highly sensitive and selective detection of bisphenol A, Talanta, 176 (2018) 595-603.

[10] L. Peyre, P. Rouimi, G. de Sousa, C. Héliès-Toussaint, B. Carré, S. Barcellini, M.-C. Chagnon, R. Rahmani, Comparative study of bisphenol A and its analogue bisphenol S on human hepatic cells: A focus on their potential involvement in nonalcoholic fatty liver disease, Food Chem. Toxicol., 70 (2014) 9-18.

[11] X. Wang, Simultaneous determination of bisphenol A and bisphenol S using multi-walled carbon nanotubes modified electrode, Food Chem. Toxicol., (2018) 11906-11922.

[12] W. Du, J. Liu, H. Li, C. Deng, J. Luo, Q. Feng, Y. Tan, S. Yang, Z. Wu, F. Xiao, Competition-based two-dimensional photonic crystal dually cross-linked supramolecular hydrogel for colorimetric and fluorescent dual-mode sensing of bisphenol A, Anal. Chem., 95 (2023) 4220-4226.

[13] D.N. Unal, S. Yıldırım, S. Kurbanoglu, B. Uslu, Current trends and roles of surfactants for chromatographic and electrochemical sensing, TrAC Trend. Anal. Chem., 144 (2021) 116418.

[14] Y. Pang, Y. Cao, J. Han, Y. Xia, Z. He, L. Sun, J. Liang, A novel fluorescence sensor based on Zn porphyrin MOFs for the detection of bisphenol A with highly selectivity and sensitivity, Food Control, 132 (2022) 108551.

[15] X. Zhang, J. Zhu, Z. Wu, W. Wen, X. Zhang, S. Wang, Electrochemical sensor based on confined synthesis of gold nanoparticles @ covalent organic frameworks for the detection of bisphenol A, Anal. Chim. Acta, 1239 (2023) 340743.

[16] K.V. Ragavan, N.K. Rastogi, M.S. Thakur, Sensors and biosensors for analysis of bisphenol-A, TrAC Trend. Anal. Chem., 52 (2013) 248-260.

[17] O. Moradi, Electrochemical sensors based on carbon nanostructures for the analysis of bisphenol A—A review, Food Chem. Toxicol., 165 (2022) 113074.

[18] Q. Chen, C. Yuan, Z. He, J. Wang, C. Zhai, D. Bin, M. Zhu, A label-free photoelectrochemical sensor of S, N co-doped graphene quantum dot (S, N-GQD)-modified electrode for ultrasensitive detection of bisphenol A, Microchim. Acta, 189 (2022) 208.

[19] F. Arduini, S. Cinti, V. Scognamiglio, D. Moscone, G. Palleschi, How cutting-edge technologies impact the design of electrochemical (bio)sensors for environmental analysis. A review, Anal. Chim. Acta, 959 (2017) 15-42.

[20] V. Karthik, P. Selvakumar, P. Senthil Kumar, V. Satheeskumar, M. Godwin Vijaysunder, S. Hariharan, K. Antony, Recent advances in electrochemical sensor developments for detecting emerging pollutant in water environment, Chemosphere, 304 (2022) 135331.

[21] Y. Shen, J. Yang, Y. Zhang, T. Zeng, Q. Wan, Fabrication of a branch-like Ni-doped ZnO/graphene nanoplatelet composite for enhanced electrochemical determination of 17β-estradiol and acetaminophen, J Electron. Mater.,, 51 (2022) 5310-5321.

[22] Z. Rahmati, M. Roushani, H. Hosseini, Hierarchical hollow sea-urchin-like Ni–Co diselenide encapsulated in N-doped carbon networks as an advanced core-shell bifunctional electrocatalyst for fabrication of nonenzymatic glucose and hydrogen peroxide sensors, Sensor Actuat. B-Chem., 324 (2020) 128730.

[23] H. Yin, L. Cui, Q. Chen, W. Shi, S. Ai, L. Zhu, L. Lu, Amperometric determination of bisphenol A in milk using PAMAM–Fe_3O_4 modified glassy carbon electrode, Food Chem., 125 (2011) 1097-1103.

[24] K. Deng, X. Liu, C. Li, Z. Hou, H. Huang, A comparative study of different Fe_3O_4-functionalized carbon-based nanomaterials for the development of electrochemical sensors for bisphenol A, Anal. Methods, 9 (2017) 5509-5517.

[25] H. Yu, C. Guo, X. Zhang, Y. Xu, X. Cheng, S. Gao, L. Huo, Recent development of hierarchical metal oxides based gas sensors: from gas sensing performance to applications, Adv. Sustain. Systems, 6 (2022) 2100370.

[26] Z. He, K. Wang, S. Zhu, L.-a. Huang, M. Chen, J. Guo, S. Pei, H. Shao, J. Wang, MOF-derived hierarchical mno-doped Fe_3O_4@C composite nanospheres with enhanced lithium storage, ACS Appl. Mater. Inter., 10 (2018) 10974-10985.

[27] S. Tajyani, A. Babaei, A new sensing platform based on magnetic Fe_3O_4@ NiO core/shell nanoparticles modified carbon paste electrode for simultaneous voltammetric determination of quercetin and tryptophan, J Electroanaly. Chem., 808 (2018) 50-58.

[28] D. Zhao, Q. Hao, C. Xu, Facile fabrication of composited Mn_3O_4/Fe_3O_4 nanoflowers with high electrochemical performance as anode material for lithium ion batteries, Electrochim. Acta, 180 (2015) 493-500.

[29] R. Nehru, C.-D. Dong, C.-W. Chen, Cobalt-doped Fe_3O_4 nanospheres deposited on graphene oxide as electrode materials for electrochemical sensing of the antibiotic drug, ACS Appl. Nano Mater., 4 (2021) 6768-6777.

[30] Y. Zhang, L. Li, H. Su, W. Huang, X. Dong, Binary metal oxide: advanced energy storage materials in supercapacitors, J Mater. Chem. A, 3 (2015) 43-59.

[31] J. Yang, H. Ye, Z. Zhang, F. Zhao, B. Zeng, Metal–organic framework derived hollow polyhedron $CuCo_2O_4$ functionalized porous graphene for sensitive glucose sensing, Sensor Actuat. B-Chem., 242 (2017) 728-735.

[32] J. Yu, Y. Zhang, H. Li, Q. Wan, Y. Li, N. Yang, Electrochemical properties and sensing applications of nanocarbons: A comparative study, Carbon, 129 (2018) 301-309.

[33] H.-W. Huang, S.-S. Fan, W. Dong, W. Zou, M. Yan, Z. Deng, X. Zheng, J. Liu, H.-E. Wang, L. Chen, Y. Li, B.-L. Su, Nitrogen-doped graphene in-situ modifying MnO nanoparticles for highly improved lithium storage, Appl. Sur. Sci., 473 (2019) 893-901.

[34] W.R.P. Barros, Q. Wei, G. Zhang, S. Sun, M.R.V. Lanza, A.C. Tavares, Oxygen reduction to hydrogen peroxide on Fe_3O_4 nanoparticles supported on printex carbon and graphene, Electrochim. Acta, 162 (2015) 263-270.

[35] J. Yang, G. Zhu, Y. Liu, J. Xia, Z. Ji, X. Shen, S. Wu, Fe_3O_4-decorated Co_9S_8 nanoparticles in situ grown on reduced graphene oxide: a new and efficient electrocatalyst for oxygen evolution reaction, Adv. Funct. Mater., 26 (2016) 4712-4721.

[36] J. Yang, X. Liu, K. Song, X. Li, D. Wang, Effectively removing tetracycline from water by nanoarchitectured carbons derived from CO_2: Structure and surface chemistry influence, Environ. Res., 195 (2021) 110883.

[37] Q. Wu, M. Jiang, X. Zhang, J. Cai, S. Lin, A novel octahedral MnO/RGO composite prepared by thermal decomposition as a noble-metal free electrocatalyst for ORR, J Mater. Sci., 52 (2017) 6656-6669.

[38] H. Kohzadi, M. Soleiman-Beigi, XPS and structural studies of Fe_3O_4-PTMS-NAS@Cu as a novel magnetic natural asphalt base network and recoverable nanocatalyst for the synthesis of biaryl compounds, Sci. Rep., 11 (2021) 24508.

[39] W. Wei, S. Yang, H. Zhou, I. Lieberwirth, X. Feng, K. Müllen, 3D graphene foams cross-linked with pre-encapsulated Fe_3O_4 nanospheres for enhanced lithium storage, Adv. Mater., 25 (2013) 2909-2914.

[40] J. Qian, J. Yang, Y. Zhang, T. Zeng, Q. Wan, N. Yang, Interfacial superassembly of flower-like NiMn-LDH@poly-l-lysine composites for selective electrochemical sensing of tryptophan, Anal. Chim. Acta, 1237 (2023) 340608.

[41] K. Ahmad, P. Kumar, S.M. Mobin, A highly sensitive and selective hydroquinone sensor based on a newly designed N-rGO/$SrZrO_3$ composite, Nanoscale Adv., 2 (2020) 502-511.

[42] A. Olejnik, K. Siuzdak, J. Karczewski, K. Grochowska, A flexible Nafion coated enzyme free glucose sensor based on Au dimpled Ti structures, Electroanalysis, 32 (2020) 323-332.

[43] A.R. Cherian, L. Benny, A. George, U. Sirimahachai, A. Varghese, G. Hegde, Electro fabrication of molecularly imprinted sensor based on Pd nanoparticles decorated poly-(3 thiophene acetic acid) for progesterone detection, Electrochim. Acta, 408 (2022) 139963.

[44] J. Zhang, X. Xu, L. Chen, An ultrasensitive electrochemical bisphenol A sensor based on hierarchical Ce-metal-organic framework modified with cetyltrimethylammonium bromide, Sensor Actuat. B-Chem., 261 (2018) 425-433.

[45] Y.-Y. Huang, Y.-H. Pang, X.-F. Shen, R. Jiang, Y.-Y. Wang, Covalent organic framework DQTP modified pencil graphite electrode for simultaneous determination of bisphenol A and bisphenol S, Talanta, 236 (2022) 122859.

[46] M.Y. Ali, A.U. Alam, M.M.R. Howlader, Fabrication of highly sensitive bisphenol A electrochemical sensor amplified with chemically modified multiwall carbon nanotubes and β-cyclodextrin, Sensor Actuat. B-Chem., 320 (2020) 128319.

[47] S.Z. Bas, N. Yuncu, K. Atacan, M. Ozmen, A comparison study of MFe_2O_4 (M: Ni, Cu, Zn)-reduced graphene oxide nanocomposite for electrochemical detection of bisphenol A, Electrochim. Acta, 386 (2021) 138519.

[48] D. Huang, X. Huang, J. Chen, R. Ye, Q. Lin, S. Chen, An electrochemical bisphenol: a sensor based on bimetallic Ce-Zn-MOF, Electrocatalysis, 12 (2021) 456-468.

[49] Y.-H. Pang, Y.-Y. Huang, L. Wang, X.-F. Shen, Y.-Y. Wang, Determination of bisphenol A and bisphenol S by a covalent organic framework electrochemical sensor, Environ. Pollut., 263 (2020) 114616.